Excess PbI_2 Management via Multimode Supramolecular Complex Engineering Enables High Performance Perovskite Solar Cells

Hengkai Zhang[1,2,5,†], Wei Yu[1,3,†], Junxue Guo[3], Chao Xu[4], Zhiwei Ren[1,2], Kuan Liu[1,2], Guang Yang[5], Minchao Qin[6], Jiaming Huang[1,2], Zhiliang Chen[1], Qiong Liang[1,2], Dong Shen[7], Zehan Wu[4], Yaokang Zhang[8], Hrisheekesh Thachoth Chandran[1,2], Jianhua Hao[4], Ye Zhu[4], Chun-sing Lee[7], Xinhui Lu[6], Zijian Zheng[8], Jinsong Huang[5*], Gang Li[1,2*]

Affiliations:

[1]Department of Electronic and Information Engineering, Research Institute for Smart Energy (RISE), The Hong Kong Polytechnic University, Hung Hom, Kowloon, Hong Kong, China.

[2]The Hong Kong Polytechnic University Shenzhen Research Institute, Shenzhen 518057, China.

[3]State Key Laboratory of Catalysis, Dalian Institute of Chemical Physics, Chinese Academy of Sciences, Dalian National Laboratory for Clean Energy, Dalian 116023, Liaoning, China.

[4]Department of Applied Physics, The Hong Kong Polytechnic University, Hung Hom, Kowloon, Hong Kong, China.

[5]Department of Applied Physical Sciences, University of North Carolina at Chapel Hill, Chapel Hill, NC, USA.

[6]Department of Physics, The Chinese University of Hong Kong, New Territories, Hong Kong, China.

[7]Center of Super-Diamond and Advanced Films (COSDAF), Department of Chemistry, City University of Hong Kong, Kowloon, Hong Kong, China.

[8]Laboratory for Advanced Interfacial Materials and Devices, Research Centre for Smart Wearable Technology, Institute of Textiles and Clothing, The Hong Kong Polytechnic University, Hung Hom, Kowloon, Hong Kong, China.

* Correspondence author. Email: jhuang@unc.edu (J.H.), gang.w.li@polyu.edu.hk (G.L.)

[†]These authors contributed equally: Hengkai Zhang and Wei Yu.

Abstract

Excess PbI_2 in perovskite film is an effective strategy for boosting perovskite solar cells (PSCs) performance. However, the presence of unreacted PbI_2 is a critical source of intrinsic instability in perovskite under illumination, due to the photolysis of PbI_2 (decomposed into metallic lead and iodine). Herein, we solve this issue by applying ionic liquids on PSCs where the ionic liquids could form types of stable supramolecules with residual lead iodide. The formation process and mechanism of supramolecules are elucidated. The residual PbI_2 is also revealed to cause high level lead interstitial defects and induced tensile strain which further deteriorate device performance. The self-assembled supramolecular complex could passivate the PSCs where significant enhancements are achieved in both PCE (from 21.9% to 23.4%) and device stability (retaining 95% of the initial PCE after 4080 h in ambient dry-air storage, and 80% after 1400 h continuous light illumination).

Introduction

Metal halide perovskite solar cells (PSCs) have achieved certified power conversion efficiency (PCE) of 25.5% within just a decade of amazing progress.[1-3] Among the various strategies adopted, the addition of excess PbI_2 (5~10 mol%) in the precursor of PSCs is a very popular strategy for efficiency enhancement (10 mol% excess PbI_2 was used in the first > 25% PSC).[1] Unreacted PbI_2 is reported to be located at the grain boundaries, the perovskite grain surface, and the interface between the perovskite and transporting layer.[4-13] The benefits of excess PbI_2 in PCE have been widely investigated and was attributed to the mechanisms such as passivating the defects at grain boundaries,

preventing the formation of organic-rich surface, reducing halide vacancy concentration, and enhancing the charge transport.[4-10] The unreacted PbI_2 formed at the interface between the perovskite layer and charge transport layer can effectively suppress carrier recombination and facilitate the carrier injection.[5,11,12] However, the presence of unreacted PbI_2 is a double-edged sword for the PSCs,[14] which is a critical source of intrinsic instability in perovskite under illumination, due to the photolysis of PbI_2 (decomposed into metallic lead and iodine).[10,15-18] It's not enough to pursue high efficiency by sacrificing the device stability with the strategy of excess PbI_2.[15,17]

Several methods have been introduced to eliminate the detrimental effect of unreacted PbI_2. Wang et al. reported a ligand-modulation technique, in which the shape and distribution of excess PbI_2 in the perovskite films were modulated from the random distribution of excess PbI_2 into vertical distributed PbI_2 nanosheets.[19] While it benefits the device performance, this distribution regulation of unreacted PbI_2 cannot change the nature of instability induced by the photolysis of PbI_2. Secondary growth method by employing organic cations (MAI, MABr, FAI, GuaBr, et al.)/IPA solution surface treatment is an effective way to eliminate the residual PbI_2 by converting it to perovskite, whose stability needs further boosting.[20-23] Therefore, efforts are required to simultaneously remove the residual PbI_2 and improve stability.

Ionic liquids (ILs) with unique advantages have been applied in PSCs to play multiple functions for efficient and stable PSCs, including film formation dynamics control, interface modification, chemical passivation, stability improvement, and innovative alternatives to traditional materials.[24,25] However, it is still unclear the

distribution of ILs in the perovskite films, and the interaction between ILs and residual PbI_2. Noticed ILs are easily interacted with lead halides and form organic-inorganic plumbate with supramolecular organizations (Here we adopt the term supramolecule from previous literature and used in the following section.).[26-32] The self-assembly supramolecules exhibit promising semiconducting property, structural rigidity, and excellent stability.[27,30-34] Thus the ultra-stable supramolecule formed from ILs and PbI_2 holds the promise to simultaneously remove the residual PbI_2 and realize stable PSCs, and provides evidence to track the distribution of ILs in perovskite film.

In this work, we used the 1-butyl-3-methylimidazolium based ionic liquids ([BMIM]X) to react with excess PbI_2 in perovskite film and form the self-assembly supramolecule complex $[BMIM]Pb_2X_5$, which is extremely stable under continuous light illumination in the ambient environment, thus efficiently eliminates the detrimental stability effect of unreacted PbI_2. This novel ionic liquid based multi-mode supramolecular complex engineering (***ILSC***) approach is shown universal in boosting device PCE by passivating Pb interstitial defects across various PSC material systems: $(FAPbI_3)_{0.95}(MAPbBr_3)_{0.05}$ perovskite (FAMA) and $(FAPbI_3)_{0.93}(MAPbI_3)_{0.04}(CsPbI_3)_{0.03}$ perovskite (FAMACs) as example here.). The FAMACs PSC with the ***ILSC*** approach ([BMIM]Br) exhibits a PCE of 23.4% (*vs* the control device of 21.9%). The PCE of FAMA PSCs was enhanced from 19.49% (control device) to 21.94% ([BMIM]Br treated device) and 22.33% ([BMIM]Cl treated device). Moreover, perovskite films with excess PbI_2 were observed to have larger tensile strain than perovskite film with stoichiometric PbI_2, which can be effectively released through

ILSC approach by curing the Pb^{2+} interstitial induced lattice distortion and eliminating the thermal expansion coefficient mismatch between perovskite and lead iodide. Through the synergetic regulations on both the detrimental excess PbI_2 and residual tensile strain, the ***ILSC*** approach enables high-stability PSCs: maintaining 95% of the initial PCE after 4080 h ambient storage in dry box and 80% of PCE after 1400 h under light illumination.

Results and discussion

Mechanism of ionic liquid on excess PbI_2 management.

In high-efficiency PSCs, excess PbI_2 (here 10%) is commonly applied as a defect passivation agent in the perovskite film.[1] However, the excess PbI_2 is also shown to increase the ionic movement and photodecomposition, deteriorating the stability of the perovskite layer[10,14,35]. To modulate the excess PbI_2 and enhance the efficiency and stability of PSCs, 1-butyl-3-methylimidazolium based ionic liquids ([BMIM]X) ionic liquid is utilized to form supramolecular organizations with PbI_2.[26-29] As illustrated in **Figure 1a**, [BMIM]Br/IPA solution is coated on $(FAPbI_3)_{0.95}(MAPbBr_3)_{0.05}$ perovskite films, then the sample is annealed at 100 ºC for 10 min to form supramolecular organization. The supramolecule is firstly demonstrated by XRD results (**Figure 1b**), that new peaks appear except the dominant peaks of α-$FAPbI_3$ ((100) at 13.95º, (111) at 24.45º, (200) at 28º), δ-$FAPbI_3$ (11.7º) and the PbI_2 peak (12.6º). The new peak at 7.9º is generated with a low concentration of [BMIM]Br (1 and 3 mg mL^{-1}), which is attributed to ***Supramolecule I*** (confirmed as the supramolecular organization of MPb_2X_5 in the following section, where M stands for the organic cation and X

represents the halide anion). When the concentration of [BMIM]Br increases to 5 mg mL^{-1}, a new peak at around 10° arises, suggesting another compound (***Supramolecule II***, also confirmed as the supramolecular organization of $MPbX_3$ in the following section) is formed. Continuously increasing [BMIM]Br to 10 mg mL^{-1}, the peak at 7.9 ° completely disappears and only the peak at 10.0° remains. These XRD results declare new compounds formed and a clear phase transformation with the increase of [BMIM]Br concentration. This phenomenon is also observed for the [BMIM]Cl-treated films (**Figure S1a**), suggesting that the $[BMIM]^+$ plays a critical role in the reaction. Moreover, both peak intensities for PbI_2 and δ-$FAPbI_3$ are reduced for [BMIM]Br-treated case, compared with the control film, indicating that the [BMIM]Br can effectively suppress the formation of non-perovskite δ-phase $FAPbI_3$ by forming new phases.

Specifically, perovskite films with different PbI_2:FAI ratios are prepared and treated with 3 mg mL^{-1} [BMIM]Br. The XRD patterns (**Figure 1c**) demonstrate that a clear new peak of ***Supramolecule I*** at 7.9° is observed in the film with PbI_2: FAI ratio of 1.2:1, while there is almost no emerging peaks for 1:1 and 0.9:1 ratios of PbI_2: FAI, indicating the supramolecule could only form with the residual PbI_2.

Confirmed by the GIWAXS results (**Figure 1e)**, after treated with [BMIM]Br, the typical perovskite phase ((100) at q of 1.0 $Å^{-1}$) remains unchanged, while the PbI_2 phase (q of 0.9 $Å^{-1}$) gradually diminishes and new phases of q = 0.56 $Å^{-1}$ and 0.68 $Å^{-1}$generate, suggesting interaction between PbI_2 and [BMIM]Br. At low [BMIM]Br concentrations (1 and 3 mg mL^{-1}), new peak appears at q = 0.56 $Å^{-1}$ (2θ peak position at 7.9°,

Supramolecule I), while with the increases of [BMIM]Br concentration, ***Supramolecule I*** transforms into a new phase at 0.68 $Å^{-1}$(2θ peak position at 10.0°) - ***Supramolecule II***, agreeing well with the XRD results.

Noted that the annealing process is necessary for the generation of supramolecular organization, as only the annealed film exhibits new XRD diffraction peaks (**Figure 1d**). The optical images (**Figure S1b)** show that the color of [BMIM]Br treated perovskite films (light gold color for 3 mg mL^{-1} [BMIM]Br treated and light purple color 5 mg mL^{-1} [BMIM]Br treated film) changed to the same color as the control one after thermal annealing, indicating the supramolecule formation upon thermal annealing on top of perovskite film, i.e., Supramolecule-Perovskite heterojunction.

Additionally, imidazolium based ILs with different lengths of alkyl chains were investigated (**Figure S2**). The XRD patterns show that compared to [BMIM]Br, 1-methyl-3-propylimidazolium bromide ([MPRIM]Br) and 1-ethyl-3-methylimidazolium bromide ([EMIM]Br) with shorter alkyl chains can only give new peaks at around 10°, while 1-methyl-3-pentylimidazolium bromide ([MPEIM]Br), 1-hexyl-3-methylimidazolium bromide ([HMIM]Br), and 1-methyl-3-octylimidaolium bromide ([OMIM]Br) with longer alkyl chains only exhibit new peaks at around 7.9°.

As shown in top-view SEM images (**Figure 1f**), the unreacted PbI_2 in the forms of brighter nanocluster is randomly distributed in the control perovskite film, which is consistent with the previous reports.[17] After treated with [BMIM]Br, instead of residual PbI_2, new features locating between the perovskite grain boundaries are observed, and the perovskite grain size becomes larger, which may be attribute to the Ostwald

ripening.[36] The grain size distribution is shown in Figure S3. The average grain size of control film is around 0.72 um. The perovskite grain size becomes larger after treatment with [BMIM]Br where the average grain size of film with Supramolecule I is 0.87 um. The enlarged grain size can be confirmed by the XRD results in Figure 1b, that the full-width at half-maximum (FWHM) of the (100) diffraction peak for 3 mg mL^{-1} and 5 mg mL^{-1} [BMIM]Br treated films are 0.211 and 0.234, respectively, lower than the control film of 0.243. According to the Scherrer's equation, the reduced FWHM reflects enlarged crystallize size for [BMIM]Br treated films. The treatment of [BMIM]Br also reduces the film roughness to 18.8 nm, where the surface roughness of control film is 34.9 nm (Figure S4).

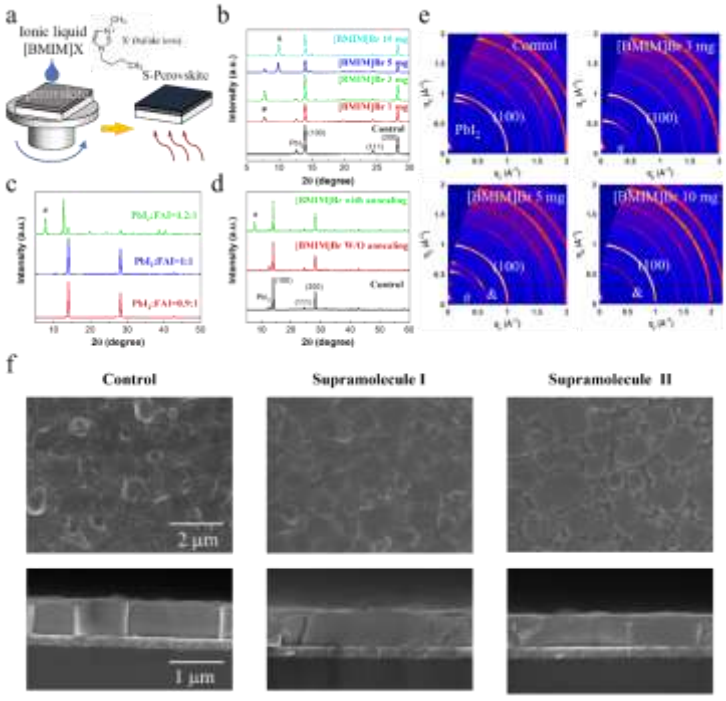

Fig. 1 Mechanism of ionic liquid on excess PbI_2 management. a) Schematical illustration of

supramolecule formation on perovskite film – supramolecule-perovskite (s-perovskite). b) XRD patterns of formation of Perovskite with different concentrations of ionic liquid. c) XRD patterns of 3 mg mL^{-1} [BMIM]Br treated perovskite film with PbI_2: FAI ratio of 1.2:1, 1:1 and 0.9:1. d) XRD patterns of 3 mg mL^{-1} [BMIM]Br modulated perovskite films with and without annealing process. e) GIWAXS patterns of the control and perovskite films for different concentrations ionic liquid. f) Top-view and cross-sectional view SEM images of control and perovskite films with Supramolecule I (3 mg mL^{-1}) and Supramolecule II (5 mg mL^{-1}).

Depth resolved investigation of excess PbI_2 over the perovskite film

As the perovskite film is treated with ionic liquid from the top surface. It is necessary to investigate the content of residual PbI_2 over the whole perovskite film (**Figure 2a**). Depth-Resolved GIWAXS measurements are first used to probe the unreacted PbI_2 content at a specific depth via changing the incident angle. Three incident angles of 0.1°, 0.3°, and 1° are selected for the top 10 nm, the middle layer of film and the whole film of GIWAXS test, respectively.[23] For the control perovskite film (**Figure 2b**), a strong PbI_2 signal at q = 0.9 $Å^{-1}$ is observed for all three incident angles, suggesting the residual PbI_2 across the whole film. In contrast, no PbI_2 signal is detected near the film surface (0.1º) for the [BMIM]Br-treated films, and only a very weak peak of the PbI_2 phase is observed at higher incident angles of 0.3º and 1.0º. In comparison, the [BMIM]Br-treated films exhibit a strong peak at q = 0.56 $Å^{-1}$ (***Supramolecule I***) regardless of incident angles, indicating that most of the excess PbI_2 was converted. Furthermore, the ratios of PbI_2 and perovskite (100) peak intensity from the depth resolved GIWAXS results are calculated for the control film (**Figure 2d)** to investigate

the PbI_2 distribution throughout the perovskite film. The ratio is two times higher in the middle layer than those in the top and bottom layers, declaring a higher content of PbI_2 in the middle of the perovskite film.

The Fourier-transform infrared spectroscopy (FTIR) and time-of-flight secondary-ion mass spectrometry (ToF-SIMS) measurement are conducted to further investigate the presence of [BMIM]Br and distribution of chemical composition throughout the ***ILSC*** perovskite films. The IR spectrum (Figure S5) of [BMIM]Br shows the characteristic IR modes at 590-690, 1080-1600 and 2800-3200 cm^{-1} (alkyl and imidazole ring C-H stretch), which is consistent with the reported by Rao et al.[37] A closer examination of IR spectra in the imidazole ring C-H stretch between 3000-3250 cm^{-1} shows that compared to the control perovskite film, new vibration at 3112, 3165 and 3199 cm^{-1} are seen for [BMIM]Br treated case, confirmed the presence of [BMIM]Br in the perovskite film. From the ToF-SIMS, the abrupt boosting of the F^- signal indicates the touching of the FTO substrate after 275 s ion sputtering (**Figure 2c**). The composition of MA^+ is linear increase at the first 47 s ion sputtering and become constant after 47 s. This indicates less MA^+ is distributed at the top surface of perovskite film, which could be attributed to the evaporation of MA during annealing process. The MA^+ at the top surface is much easier released than the MA^+ at the middle or bottom layer of perovskite film. The compositions of FA^+ and Pb^{2+} are almost constant over the whole perovskite film, while there exist three regions of $[BMIM]^+$ throughout the film: I. Initial/top drop region; II. Accumulation region; and III. Final/bottom drop region (**Figure 2a** and **2c**). Physically, the [BMIM]Br is first coated onto the surface of

the perovskite film and then diffuses into the bulk of the film. According to the typical diffusion process, the first linear drop (before 47 s, mainly on the film surface) and the final/bottom drop (III, after 150 s) regions are easy to understand. The existence of accumulation region (II. 47-150 s) is however very interesting since the $[BMIM]^+$ is abnormally increasing and accumulated in the middle of the film. The distribution of unreacted PbI_2 in the film, as confirmed by the depth resolved GIWAXS analysis (**Figure 2d**), may provide insight in understanding the abnormal $[BMIM]^+$ distribution. If the [BMIM]Br reacts with PbI_2, the accumulation of PbI_2 will result in the accumulation of $[BMIM]^+$ in the middle of perovskite film. In this scenario, the $[BMIM]^+$ can track the unreacted PbI_2 and the ***ILSC*** is a powerful approach to eliminate the unreacted PbI_2 not only on the surface but also in the bulk of perovskite film.

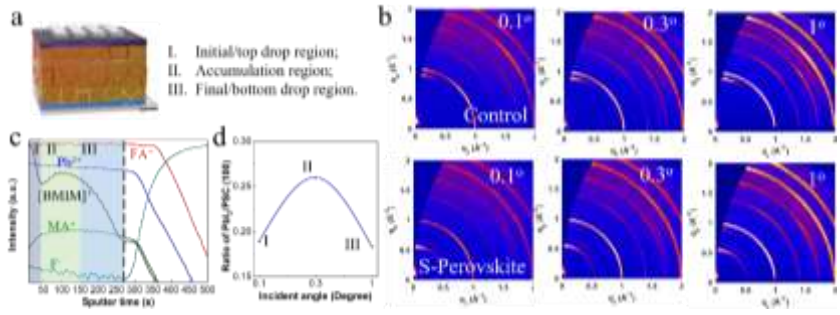

Fig. 2 Depth resolved investigation of excess PbI_2 through perovskite film. a) Schematic diagram of the proposed three regions of supramolecule and excess PbI_2 distributed on perovskite film. b) Depth resolved GIWAXS pattern of control film and S-Perovskite. c) ToF-SIMS depth profiles of the S-Perovskite film over sputtering time. d) The calculated PbI_2/PSC (100) ratio from depth resolved GIWAXS pattern of control film.

Formation of supramolecule via ionic liquid and the DFT calculation

To understand the mechanism and figure out the structures of two ***Supramolecules I*** and ***II***, films were made by spin-coating with different ratios of PbI_2 and [BMIM]Br. As the XRD results shown in **Figure 3g**, two main peaks located at 7.9° and 10° are found for the films of ***Supramolecule I*** ([BMIM]Pb_2I_4Br, PbI_2:[BMIM]Br=2:1) and ***Supramolecule II*** ([BMIM]PbI_2Br, PbI_2:[BMIM]Br=1:1), respectively, exactly the same with the peaks of ***Supramolecule*** on perovskite film shown in **Figure 1b**. The corresponding GIWAXS (**Figure 3e** and **f**) shows clear bright Bragg spots around q of 0.56 $Å^{-1}$ and 0.68 $Å^{-1}$ for the ***Supramolecules I*** and ***II***, respectively, representing the detailed crystallographic information of ***Supramolecule I*** and ***II*** in the films. These results demonstrated that ***Supramolecule I*** and ***II*** are the reaction products of [BMIM]Br and PbI_2.

The structures of ***Supramolecule I*** and ***II*** are then investigated through the single crystal TEM measurement. Based on the previous reference on ionic liquid based supramolecule, we propose the structures of two supramolecules in **Figure 3a** and **3b**. [27,33] To confirm, we further compare the experimental TEM diffraction figure (left) of the single crystal supramolecules with the simulated TEM diffraction figure (right) of the proposed structures (**Figure 3c** and **3d**). The obtained experimental TEM diffraction patterns match the proposed structures exactly. Therefore, we confirm the proposed structures as: ***Supramolecule I*** ([BMIM]Pb_2I_4Br) comprises sheets of corner and edge sharing lead iodide octahedra, separated by $[BMIM]^+$ cations which form stacks perpendicular to the anionic slabs; The ***Supramolecule II*** ([BMIM]PbI_2Br) consists of one Pb^{2+} and one $[BMIM]^+$ organic cation, where the 1D Pb-I(Br)-Pb chain is formed

as inorganic skeleton surrounded by the $[BMIM]^+$ cations.

Combined with the XRD results of perovskite films from ionic liquid with different alkyl chain lengths, the basic rules of supramolecular organization formation are proposed (**Figure S6**). For the imidazolium cations with longer alkyl chains, it tends to self-assemble into MPb_2X_5 Supramolecule I with lead halides. While for the imidazolium cations with shorter alkyl chains, Supramolecule II $MPbX_3$ is preferably formed during the reaction with lead halides. The connection between alkyl chain length and Supramolecular organization structure is possibly linked to the thermodynamic stability of the self-assemble process. During the self-assemble process, the organic cation can be inserted into the space of two parallel Pb-X-Pb chains (or walls). The space between two parallel Pb-X-Pb chains has a range between maximum distance and minimum distance (D_{max} to D_{min}). For the organic cations with different size of (R_{cation}), three conditions exhibit: a. if $2R_{cation} > D_{max}$ & $R_{cation} > D_{min}$, ***Supramolecule I*** will form; b. if $2R_{cation} < D_{max}$ & $R_{cation} < D_{min}$, ***Supramolecule II*** will form; and c. if $2R_{cation} < D_{max}$ & $R_{cation} > D_{min}$, both ***Supramolecule I*** and ***II*** are thermodynamic stable and formation structures are determined by the ratio of organic cation and lead halide. Therefore, the proper alkyl chain length of $[BMIM]^+$ results in an interesting concentration-dependent phase transformation from ***Supramolecule I*** to ***II*** with the reduced PbI_2:[BMIM]X ratio (2:1 to 1:1). The UV-vis absorption spectra were shown in Figure S7a, that all the supramolecules I are at drop stage at 360 nm, while the absorption of supramolecule II shows an opposite behavior. Besides, at 390 nm, the supramolecule II drops sharply and supramolecule I rise. Therefore, we believe

this phenomenon is a normal observation.

The reaction between [BMIM]Br and PbI_2 is then studied by X-ray photoelectron spectroscopy (XPS). The typical C 1s and N 1s spectra of the control and [BMIM]Br-treated perovskite films (**Figure S8**) clearly show a strong $C{=}NH_2^+$ peak corresponding to FA^+ in perovskites. However, the presence of π–π peak and the intensity of $C\text{-}NH_2$ (~ 286 eV for C 1s and ~ 401.5 eV for N 1s) arises in the [BMIM]Br-treated perovskite film and ***Supramolecule I*** [BMIM]Pb_2I_4Br film (**Figure S9**), verifying the formation of supramolecules in perovskite film. The XPS core-level energy spectra of Pb 4f for the control perovskite film show two main peaks at 138.79 and 143.73 eV, corresponding to the Pb $4f_{7/2}$ and Pb $4f_{5/2}$. The shifts of the Pb^{2+} peaks to lower binding energy for [BMIM]Br treated perovskite films (138.29 and 143.23 eV) and ***Supramolecule I*** [BMIM]Pb_2I_4Br films (138.73 and 143.67 eV), indicate the lowered oxidation state of lead, which is attributed to the formation of [BMIM]Pb_2I_4Br.[38-40]

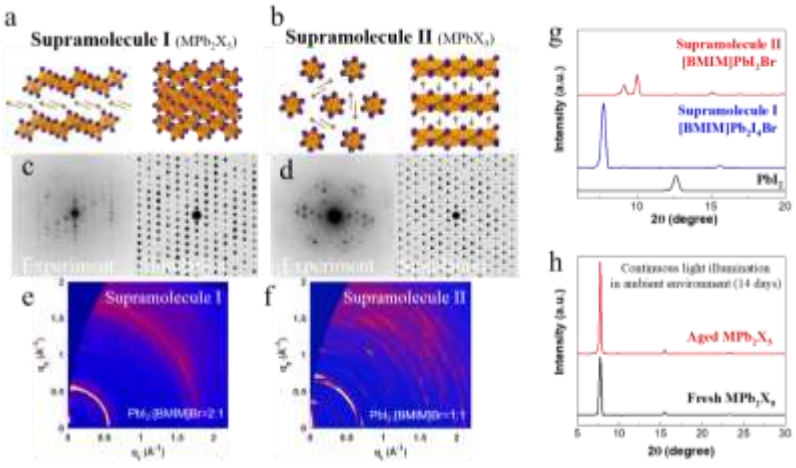

Fig. 3 The supramolecules formation via ionic liquid on PbI_2 management. Ionic liquid based supramolecular organization: a) Supramolecule I MPb_2X_5 and b) Supramolecule II $MPbX_3$.

Comparison TEM diffraction pattern image of experiment results (left) and simulation (right) of c) Supramolecule I MPb_2X_5 and d) Supramolecule II $MPbX_3$. GIWAXS patterns of e) Supramolecule I and f) Supramolecule II. g, XRD patterns of two types Supramolecule. h) XRD of fresh and aged Supramolecule I under continuous light illumination. M represents the imidazolium cation, and X is the halogen anion.

Regarding the electronic structures, we apply the density functional theory (DFT) to investigate the better device performance of Supramolecule I-based PSCs. **Figure 4a** shows a bandgap around 2.14 eV for Supramolecule I, which is close to the experimental results. Notably, the localized empty states next to the conduction band minimum (CBM) are located at Ev + 1.82 eV (EV denotes 0 eV). With the introduction of the empty states, the intrinsically direct bandgap turns into the indirect bandgap due to the change of CBM from Γ point to C after the introduction of ionic liquids. Meanwhile, we also notice the downshifts of valence band maximum (VBM) of 0.32 eV, which is attributed to the compression effect induced by the $[BMIM]^+$ layers. Then, the total density of states (TDOS) and partial density of states (PDOS) are demonstrated to reveal the orbital contributions (**Figure 4b**). For the VBM, it is noted that the I-5p orbitals play the dominant role, where the Pb-6s orbitals also show a slight contribution. The C-2p orbitals locate at a deep position in the conduction band with an electronic inactive feature, supporting a weak influence on the conductivity. Br-4p orbitals are mostly located at the lower position of VBM, which mainly comes from the [BMIM]Br. This is potentially induced by the long-range p-p orbital coupling effect between the Br-4p orbitals and Pb-6p orbitals in Supramolecule I. This indicates the introduction of

[BMIM]Br layers will influence the electronic structures of perovskite. The empty states induced by the $[BMIM]^+$ layers mainly consist of the N-2p orbitals. Meanwhile, Pb-6p dominates the CBM with minor contributions from I-5p. It is found that C-2p orbitals show an obvious contribution near the CBM, indicating the coupling between the Pb-X-Pb walls and the ionic liquids. Additionally, **Figure 4c-d** shows the highest occupied molecular orbital (HOMO) and lowest unoccupied molecular orbital (LUMO), respectively, where the HOMO is dominated by Pb-X-Pb walls while the LUMO mainly locates at the $[BMIM]^+$ layers. More importantly, the limited overlapping of HOMO and LUMO indicates the limited electronic recombination trend between the holes and electrons, leading to the improved energy conversion efficiency of the solar cells. Therefore, these results confirm that the introduction of ionic liquid not only shows an evident interaction with PbI_2 but also demonstrates a significant effect in modulating the electronic structures of the perovskite materials.

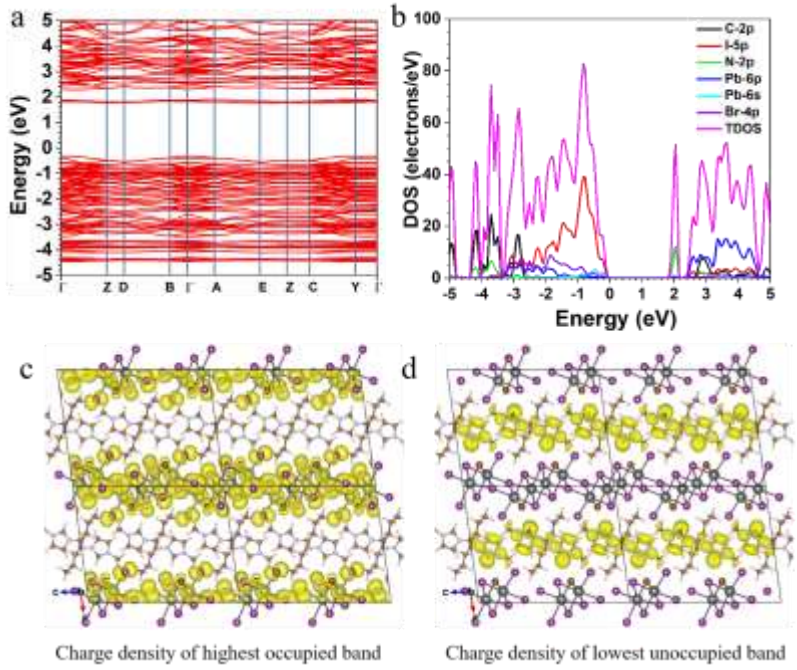

Fig. 4 DFT calculation of Supramolecule I (MPb_2X_5): a) the band structure, b) the PDOS and TDOS, c) charge density of highest occupied band (HOMO) and d) charge density of lowest unoccupied band (LUMO).

Photovoltaic and optoelectronic properties of PSCs

The PSCs are then fabricated with the device configuration of glass/FTO/SnO_2/$(FAPbI_3)_{0.95}(MAPbBr_3)_{0.05}$/Spiro-OMeTAD/Au. The detailed experimental information can be found in the experimental section. The optimized FAMA-based PSCs are found to be with 3 mg mL^{-1} [BMIM]Br (**Figure S10a** and **Table S1**), yielding a PCE of 21.94% with a short circuit current (J_{SC}) of 24.8 mA cm^{-2}, an open-circuit voltage (V_{OC}) of 1.14 V, and an FF of 77.5%. By comparison, the control device shows PCE of 19.5%, J_{SC} of 24.2 mA cm^{-2}, V_{OC} of 1.08 V, and FF of 74.9%. The

forward and reverse-scan results (**Figure 5a** and **Table S2**) indicate a negligible hysteresis for the devices. The external quantum efficiency (EQE) spectra (**Figure 5b** and **Figure S10b**) give the integrated J_{SC} values of 23.5 and 23.6 mA cm^{-2} for the control and optimized ***ILSC*** devices, respectively, which are in good agreement with the values from *J-V* curves (within 5% deviation). The steady-state power output (SPO) measurements in 500 s (**Figure 5c**) present a stable SPO PCE of 19.5% for the control and 21.4% for ***ILSC*** PSCs, respectively. Apart from [BMIM]Br, [BMIM]Cl is also used and the general modulation effect through ***ILSC*** is further confirmed (**Figure S11** and **Table S3**). The optimized [BMIM]Cl treated PSC (3 mg mL^{-1} [BMIM]Cl), exhibiting a PCE of 22.33%, J_{SC} of 24.8 mA cm^{-2}, V_{OC} of 1.14 V, and FF of 79.0%, is also on the higher side compared to the control PSCs. The statistic distribution of the photovoltaic parameters (**Figure S12**) presents the reproducibility of the V_{OC} and FF enhancement through the ***ILSC*** approach. The enhanced V_{OC} and FF of [BMIM]Br modulated devices (average of 1.126 V and 75.0%) and [BMIM]Cl based ones (average of 1.13 V and 76.5%) than the control devices (average of 1.09 V and 74.5%) result in the improved average PCE for the ***ILSC*** devices ([BMIM]Br of 20.5%, [BMIM]Cl of 21.0% *vs* control of 19.6%).

To figure out its applicability on another perovskite system, the FA dominant system - $FA_{0.93}MA_{0.04}Cs_{0.03}$-based PSCs is prepared with ***ILSC*** approach (**Figure 5d** and **Table S4**). The control device shows the PCE of 21.7%, J_{SC} of 24.3 mA cm^{-2}, V_{OC} of 1.17 V, and FF of 76.9%. With the addition of Cs, the control device of FAMACs system exhibited an enhanced *V*oc from 1.08 to 1.17 over the FAMA system PSCs. The

incorporation of Cs in $FAPbI_3$ can greatly reduce the Gibbs free energy thereby stabilizing the perovskite phase.[41] Besides a more stable perovskite phase, Cs incorporation could also reduce the impurity phase, enhance photogenerated carrier lifetime and lowers the density of trap states, leading to an enhancement of PSC's performance.[42] After ***ILSC*** approach, the ***FAMACs ILSC*** device exhibits 30 mV V_{OC} enhancement over the control one, affording a PCE of 23.4%, J_{SC} of 24.7 mA cm^{-2}, V_{OC} of 1.20 V, and FF of 79.0%. The corresponding EQE of ***FAMACs ILSC*** device is around 24.3 mA cm^{-2} which is in good agreement with the J_{SC} from *J-V* curves (within 5% deviation, **Figure 5e**). Moreover, the ***ILSC*** devices based on FAMACs perovskite using ionic liquid with different alky chains in cation ([EMIM]Br, [MPRIM]Br, [MPEIM]Br, [HMIM]Br and [OMIM]Br) were fabricated. The obtained devices exhibit obvious performance boosting with above mentioned ionic liquids, especially the V_{OC} enhancement (20 mV ~30 mV) (**Figure S13** and **Table S5**). In order to figure out the origin of performance enhancements, we also prepared the perovskite solar cell without post annealing process. As we mentioned before the post annealing process is necessary to form supramolecules (Figure 1d), the supramolecules present in the post-annealed devices, and no supramolecules will form in the devices without post-annealing. **Figure S13b** and **S13c** shows that both [BMIM]Br treated FAMA- and FAMACs-based PSCs with post-annealing gives obviously improved performances to the ones without post-annealing, demonstrating the positive contribution of supramolecules to the device performance improvement. The slightly enhancement for [BMIM]Br treated PSCs without post annealing compared to the control cases is also achieved and may

attributed to the passivation function.

The ultraviolet photoelectron emission spectroscopy (UPS) technique was applied to investigate the electronic structure of the perovskite film with [BMIM]Br (**Figure 5f**). The calculated work function (WF) for [BMIM]Br-treated perovskite film decreases to 4.56 eV from 4.83 eV (control case), yielding the HOMO level of 5.50 eV ([BMIM]Br-treated) *vs.* 5.86 eV (control). The WF (3.22 eV) and HOMO (5.61 eV) level of Supramolecule I are calculated from UPS spectra in **Figure S7b**. The corresponding Tauc plots according to the $(\alpha h\nu)^2$ versus energy (**Figure S14a**) give bandgaps (E_gs) of 1.51, and 1.52 eV for the control and [BMIM]Br modulated films, respectively. Then the LUMO levels are calculated to be 3.98 eV ([BMIM]Br-treated) and 4.35 eV (control). The shifting of HOMO and LUMO level of [BMIM]Br-treated perovskite film could be attributed the formation of Supramolecule-Perovskite heterojunction at the interface. As the HOMO level of spiro-OMeTAD is reported to be ~ 5.22 eV,[43] the [BMIM]Br treatment case reduces the energy barrier between perovskite and spiro-OMeTAD (**Figure 5g**). This energy level shift improves the hole collection and block undesirable electron transfer from the perovskite to the spiro-OMeTAD, benefiting both V_{OC} and FF.

Furthermore, the dependence of V_{OC} and J_{SC} on the light intensity is examined. The V_{OC} *vs.* light intensity curves (**Figure S14b**) state that the V_{OC} is proportional to the logarithm of light intensity, and the slopes are calculated to be 1.60 k_BT/q for the control and 1.38 k_BT/q for the ***ILSC*** PSCs, respectively, where k_B is the Boltzmann constant, T is the absolute temperature in Kelvin and q is the elementary charge. The decreased

slope from the control device to [BMIM]Br treated devices signifies that [BMIM]Br could effectively suppress the trap-assisted recombination, consistent with the 60 mV V_{OC} enhancement. The J_{SC} versus light intensity curves on a double-logarithmic scale (**Figure S14c**) can be fitted according to the relation of $J_{SC} \propto \Phi^{\alpha}$, where Φ corresponds to the light intensity and α to the exponent. The calculated α values are 0.96 for the control, and 0.97 for the [BMIM]Br ***ILSC*** PSCs, respectively, declaring the reduced bimolecular recombination in ***ILSC*** PSCs. The trap density variation of the devices is calculated by the space limited current (SCLC) method. Figure S15 shows the trap-filling limited voltage (V_{TFL}) of the control and [BMIM]Br-treated device is 0.23 and 0.17 V, respectively. The corresponding trap density can be calculated using $V_{TFL} = (qn_{trap}L^2) / (2\varepsilon\varepsilon_0)$, where q is the elementary charge, L is the thickness of the perovskite film (850 nm), ε_0 is the permittivity in vacuum (8.85×10^{12} F m^{-1}), and ε is the relative dielectric constant of $FAPbI_3$ (46.9). The trap densities n_{trap} of the control, and [BMIM]Br devices are 1.65×10^{15}, and 1.22×10^{15} cm^{-3}, respectively. The lower trap density for [BMIM]Br-treated film indicates improved film quality and passivation effect.

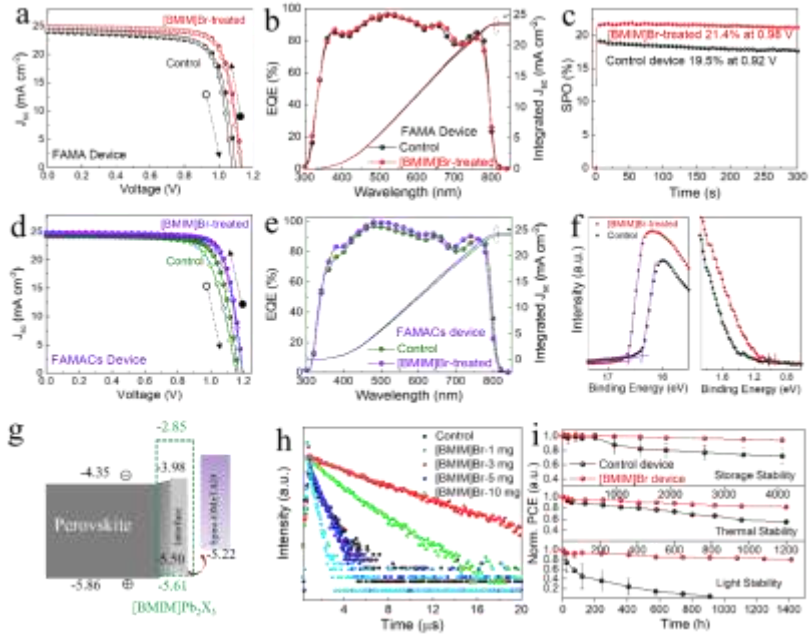

Fig. 5 Photovoltaic and optoelectronic properties of PSCSs. FAMA-based PSCs: a) *J-V* characterization, b) corresponding EQE spectra and c) the steady-state power output (SPO) of the control and [BMIM]Br-treated devices. FAMACs-based PSCs: d) *J-V* characterization and e) EQE of the control and [BMIM]Br-treated devices. f) UPS of the control and [BMIM]Br-treated FAMA perovskite films. g) The energy level diagram of the used materials. h) Time-resolved photoluminescence (TRPL) analysis of perovskite films with [BMIM]Br in different concentrations. i) Stability of the control and [BMIM]Br treated devices (the statistical data of each condition are collected from 5 devices).

The charge carrier dynamics of the perovskite films were then studied by time-resolved photoluminescence (TRPL, **Figure 5h**) and the steady-state photoluminescence (PL, **Figure S14d**). The TRPL decay profiles were fitted using a bi-exponential decay model ($Y = A_1\exp(-t/\tau_1) + A_2\exp(-t/\tau_2)$) (**Table S6**).

Compared to the control film, the optimized 3 mg mL^{-1} [BMIM]Br treated film shows the longest TRPL decay overall lifetime, and the highest PL intensity with a blue peak shift of ~ 14 nm, consistent with a reduced density of trap sites in the [BMIM]Br-treated devices.

Stability is at the center of PSC research, and tensile strain has been proposed to be another important perovskite instability source recently.[44,45] Grazing incident X-ray diffraction (GIXRD) technique with 2θ-$\sin^2\psi$ method is applied to investigate the strain in the perovskite film (detailed information see the Supporting Information). The plane (012) at 31.6° (for the minimal overlap on the high-angle side) is selected for stress analysis by varying ψ from 0° to 50° (**Figure 6a-d**), and the slopes of the 2θ-$\sin^2\psi$ linear fitting is shown in **Figure 6e**. For control films with both stoichiometric ratio and excess PbI_2, the scattering peaks gradually shift to the smaller 2θ with the increase of ψ angle, indicating the increase of crystal plane distance $d_{(012)}$ and the tensile stress bearing in these films. The 2θ-$\sin^2\psi$ linear fitting shows a larger slope in the film with excess PbI_2 (-0.033) than the stoichiometric ratio one (-0.015), suggesting the film with excess PbI_2 suffers from severer tensile stress. This could be attributed to several reasons: a. the excess PbI_2 causes a high density of lattice distortion by the Pb interstitial (**Figure 6f**); b. the lattice constant mismatch and thermal expansion coefficients difference between PbI_2 (>8 $10^{-5}K^{-1}$) [46] and perovskite (~4 $10^{-5}K^{-1}$).[47-49] The DFT calculation of Pb interstitial formation energy (**Figure 6g**) shows that much lower formation energy of Pb interstitial is required for the excess PbI_2 perovskite (inside the range of circle), indicating the Pb interstitial tends to form in the film with excess PbI_2.

Though PSCs with excess PbI_2 obtained higher PCEs, the severer tensile strain caused by excess PbI_2 has an adverse side effect on film stability.

Interestingly, with the ***ILSC*** approach, the perovskite films with stoichiometric ratio PbI_2 and with excess PbI_2 both exhibit tensile stress relaxation behavior - the scattering peaks shift toward higher 2θ angle, and the slopes of linear fitted 2θ-$\sin^2\psi$ change to positive values. These results indicate that [BMIM]Br reacts with the unreacted PbI_2, forming supramolecules, then regulating the strain during the annealing process. The modulation of PbI_2 by forming a new stable supramolecule efficiently cures the lattice distortion and releases the perovskite residual tensile strain. In the optimized condition, it even produces compression strain, and thus greatly enhances the intrinsic perovskite stability, as illustrated in the PSCs stability results below. The relaxed strain is further confirmed by Williamson-Hall analysis (**Figure S16**) from the XRD patterns in Figure 1b, as the slope of the fitted line for [BMIM]Br treated film becomes positive (0.000339) compared to the control case of negative (-0.000156).

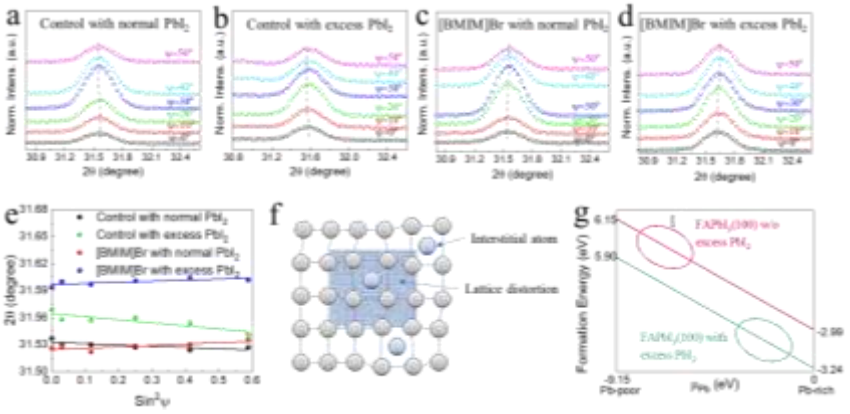

Fig. 6 GIXRD with different instrumental ψ values (10°-50°) for a) control film with stoichiometric

ratio PbI_2, b) control film with excess PbI_2, and c) [BMIM]Br modulated films with stoichiometric ratio PbI_2 and d) [BMIM]Br modulated films with excess PbI_2. e) Linear fit of 2θ-$\sin^2\psi$ for the measured films. f) Schematical illustration of interstitial atom (Pb) induced lattice distortion. g) DFT calculated defect (Pb interstitial) formation energy as a function of lead chemical potential.

Then the stability of perovskite films and PSCs are studied (**Figure 5i).** The storage-stability test was conducted on the non-encapsulated PSC devices by storing in a dark dry box with 20~30% relative humidity at room temperature. For the storage-stability, the performance of both control and ILSC devices exhibited a fluctuating performance that first increased and then decreased. The increasing of devices performance at first several days was due to the boosting of conductivity of lithium salts doped Spiro-OMeTAD during the oxidation process under storage condition[50]. The ***ILSC*** devices maintain 94% of their initial PCE after 4000 h storage, while the control case only retains 72% of PCE. For thermal stability, the devices were placed onto 80 ºC hotplate in the N_2 filled glove box. The ***ILSC*** devices exhibit a much-enhanced thermal stability (81% of its initial PCE) over the control devices (55% of initial PCE) after 1200 h thermal annealing. The light stability results were obtained by exposing the encapsulated devices under a white light-emitting diode array with an equivalent light intensity of 1 sun AM 1.5G in the air. In contrast to the rapid PCE decrease of the control devices, the ***ILSC*** PSCs exhibit greatly enhanced light stability, maintaining over 80% of their initial PCE after 1400 h light exposure. The ***ILSC*** approach effectively eliminate the lead iodide's photolysis and released the tensile strain by forming a stable [BMIM]Pb_2I_4Br supramolecule, greatly increasing the perovskite light stability. The

corresponding stability results on J_{SC}, V_{OC} and FF can be found in **Figure S17**.

The significantly improved long-term stability of [BMIM]Br treated PSCs can be explained by the highly stable of the ***Supramolecule I*** ([BMIM]Pb_2I_4Br). By keeping the ***Supramolecule I*** under continuous light illumination in an ambient environment with high relative humidity of 70%, the XRD results (**Figure 3g**) of the 14 days aged film exhibit the same peaks as the fresh sample, indicating the excellent stability of [BMIM]Pb_2I_4Br under illumination in a high humidity environment.[32]

The enhanced hydrophobicity of the [BMIM]Br-treated film further guarantees the improved stability (**Figure S18)**. The contact angle for the [BMIM]Br treated film (57.5^o) is enhanced over the control case (28.7^o), resulting in the maintained dark black color in much longer time for the treated film (over 168 h) than the control one (less than 120 h). A similar phenomenon is seen for the perovskite films covered with spiro-OMeTAD - the control film shows clear water drop spread with time, while the [BMIM]Br treated film keeps black color after 144 h without spreading of the water drop spot.

Conclusion

A stable supramolecular organization modulating strategy - ***ILSC*** is developed to regulate the unreacted PbI_2 in perovskite film, which plays dual beneficial roles - modulating excess PbI_2 and regulating tensile strain. The [BMIM]Br is found to effectively modulate PbI_2 to form a very stable complex of [BMIM]Pb_2I_4Br, enabling the ***ILSC*** devices with reduced perovskite film defect density and suppressed recombination, affording device PCE enhanced to 23.4%. Moreover, through the ILSC

approach, the excess PbI_2 is greatly reduced where the lead iodide photolysis is effectively eliminated, and the tensile strain is released, leading to significantly enhanced long-term and light stability for the [BMIM]Br PSCs.

References

1 Yoo, J. J. *et al.* Efficient perovskite solar cells via improved carrier management. *Nature* **590**, 587-593 (2021).

2 Cai, B., Xing, Y., Yang, Z., Zhang, W.-H. & Qiu, J. High performance hybrid solar cells sensitized by organolead halide perovskites. *Energy & Environmental Science* **6**, 1480-1485 (2013).

3 Kojima, A., Teshima, K., Shirai, Y. & Miyasaka, T. Organometal halide perovskites as visible-light sensitizers for photovoltaic cells. *Journal of the American Chemical Society* **131**, 6050-6051 (2009).

4 Park, B.-w. *et al.* Understanding how excess lead iodide precursor improves halide perovskite solar cell performance. *Nature communications* **9**, 1-8 (2018).

5 Chen, Q. *et al.* Controllable self-induced passivation of hybrid lead iodide perovskites toward high performance solar cells. *Nano letters* **14**, 4158-4163 (2014).

6 Kim, Y. C. *et al.* Beneficial effects of PbI2 incorporated in organo-lead halide perovskite solar cells. *Advanced Energy Materials* **6**, 1502104 (2016).

7 Dunfield, S. P. *et al.* From defects to degradation: a mechanistic understanding of degradation in perovskite solar cell devices and modules. *Advanced Energy Materials*, 1904054 (2020).

8 Bi, D. *et al.* Efficient luminescent solar cells based on tailored mixed-cation perovskites. *Science advances* **2**, e1501170 (2016).

9 Cao, D. H. *et al.* Remnant PbI2, an unforeseen necessity in high-efficiency hybrid perovskite-based solar cells? *Apl Materials* **2**, 091101 (2014).

10 Liu, F. *et al.* Is excess PbI2 beneficial for perovskite solar cell performance? *Advanced Energy Materials* **6**, 1502206 (2016).

11 Roldán-Carmona, C. *et al.* High efficiency methylammonium lead triiodide perovskite solar cells: the relevance of non-stoichiometric precursors. *Energy & Environmental Science* **8**, 3550-3556 (2015).

12 Nakayashiki, S., Daisuke, H., Ogomi, Y. & Hayase, S. Interface structure between titania and perovskite materials observed by quartz crystal microbalance system. *Journal of Photonics for Energy* **5**, 057410 (2015).

13 Yang, G. *et al.* Stable and low-photovoltage-loss perovskite solar cells by multifunctional passivation. *Nature Photonics* **15**, 681-689, doi:10.1038/s41566-021-00829-4 (2021).

14 Jacobsson, T. J. *et al.* Unreacted PbI2 as a double-edged sword for enhancing the

performance of perovskite solar cells. *Journal of the American Chemical Society* **138**, 10331-10343 (2016).

15 Tumen-Ulzii, G. *et al.* Detrimental Effect of Unreacted PbI2 on the Long-Term Stability of Perovskite Solar Cells. *Advanced Materials* **32**, 1905035 (2020).

16 Schoonman, J. Organic–inorganic lead halide perovskite solar cell materials: a possible stability problem. *Chemical Physics Letters* **619**, 193-195 (2015).

17 Roose, B., Dey, K., Chiang, Y.-H., Friend, R. H. & Stranks, S. D. Critical assessment of the use of excess lead iodide in lead halide perovskite solar cells. *The Journal of Physical Chemistry Letters* **11**, 6505-6512 (2020).

18 Juarez-Perez, E. J. *et al.* Photodecomposition and thermal decomposition in methylammonium halide lead perovskites and inferred design principles to increase photovoltaic device stability. *Journal of Materials Chemistry A* **6**, 9604-9612 (2018).

19 Wang, H. *et al.* Ligand-Modulated Excess PbI2 Nanosheets for Highly Efficient and Stable Perovskite Solar Cells. *Advanced Materials* **32**, 2000865 (2020).

20 Luo, D. *et al.* Enhanced photovoltage for inverted planar heterojunction perovskite solar cells. *Science* **360**, 1442-1446 (2018).

21 Kogo, A., Miyadera, T. & Chikamatsu, M. Tuning methylammonium iodide amount in organolead halide perovskite materials by post-treatment for high-efficiency solar cells. *ACS applied materials & interfaces* **11**, 38683-38688 (2019).

22 Hu, Z. *et al.* Enhancing the Efficiency and Stability of Triple-Cation Perovskite Solar Cells by Eliminating Excess PbI2 from the Perovskite/Hole Transport Layer Interface. *ACS Applied Materials & Interfaces* **12**, 54824-54832, doi:10.1021/acsami.0c17258 (2020).

23 Qin, M. *et al.* Precise Control of Perovskite Crystallization Kinetics via Sequential A-Site Doping. *Advanced Materials* **32**, 2004630 (2020).

24 Niu, T. *et al.* Ionic Liquids-Enabled Efficient and Stable Perovskite Photovoltaics: Progress and Challenges. *ACS Energy Letters* **6**, 1453-1479, doi:10.1021/acsenergylett.0c02696 (2021).

25 Bai, S. *et al.* Planar perovskite solar cells with long-term stability using ionic liquid additives. *Nature* **571**, 245-250 (2019).

26 Roy, S. R. & Chakraborti, A. K. Supramolecular assemblies in ionic liquid catalysis for aza-Michael reaction. *Organic letters* **12**, 3866-3869 (2010).

27 Thirumurugan, A. & Rao, C. Supramolecular organization in lead bromide salts of imidazolium-based ionic liquids. *Crystal Growth and Design* **8**, 1640-1644 (2008).

28 Craig, S. L. From ionic liquids to supramolecular polymers. *Angewandte Chemie International Edition* **48**, 2645-2647 (2009).

29 Shen, N.-N. *et al.* Supramolecular organization of [TeCl6] 2–with ionic liquid cations: studies on the electrical conductivity and luminescent properties. *Inorganic chemistry* **57**, 5282-5291 (2018).

30 Sun, C., Wang, M.-S. & Guo, G.-C. Covalently Bonded Pillared Layered Bromoplumbate with High Thermal Stability: High Capacitance Gain after Photoinduced Electron Transfer. *ACS applied materials & interfaces* **11**, 30713-30718 (2019).

31 Niu, J.-P. *et al.* Ionothermal synthesis, structure and optical properties of three new organic–inorganic hybrid imidazolium bromoplumbate complexes. *Inorganic Chemistry Communications* **14**, 663-666 (2011).

32 Sun, C. *et al.* Design strategy for improving optical and electrical properties and stability of lead-halide semiconductors. *Journal of the American Chemical Society* **140**, 2805-2811 (2018).

33 Evans, H. A. *et al.* (TTF) Pb2I5: a radical cation-stabilized hybrid lead iodide with synergistic optoelectronic signatures. *Chemistry of Materials* **28**, 3607-3611 (2016).

34 Scott, B., La Placa, S., Torrance, J., Silverman, B. & Welber, B. The crystal chemistry of organic metals. Composition, structure, and stability in the tetrathiafulvalinium-halide systems. *Journal of the American Chemical Society* **99**, 6631-6639 (1977).

35 Holovský, J. *et al.* Lead halide residue as a source of light-induced reversible defects in hybrid perovskite layers and solar cells. *ACS Energy Letters* **4**, 3011-3017 (2019).

36 Yang, M. *et al.* Facile fabrication of large-grain CH 3 NH 3 PbI 3− x Br x films for high-efficiency solar cells via CH 3 NH 3 Br-selective Ostwald ripening. *Nature communications* **7**, 1-9 (2016).

37 Rajkumar, T. & Rao, G. R. Synthesis and characterization of hybrid molecular material prepared by ionic liquid and silicotungstic acid. *Materials Chemistry and Physics* **112**, 853-857 (2008).

38 Luo, C. *et al.* Passivation of defects in inverted perovskite solar cells by imidazolium-based ionic liquid. *Sustainable Energy & Fuels* **4**, 3971-3978 (2020).

39 Wang, S. *et al.* Water-Soluble Triazolium Ionic-Liquid-Induced Surface Self-Assembly to Enhance the Stability and Efficiency of Perovskite Solar Cells. *Advanced Functional Materials* **29**, 1900417 (2019).

40 Zhu, X. *et al.* High-efficiency perovskite solar cells with imidazolium-based ionic liquid for surface passivation and charge transport. *Angew. Chem. Int. Ed.* **60**, 4238-4244, doi:10.1002/anie.202010987 (2020).

41 Yi, C. *et al.* Entropic stabilization of mixed A-cation ABX 3 metal halide perovskites for high performance perovskite solar cells. *Energy & Environmental Science* **9**, 656-662 (2016).

42 Tang, S., Huang, S., Wilson, G. J. & Ho-Baillie, A. Progress and opportunities for Cs incorporated perovskite photovoltaics. *Trends in Chemistry* **2**, 638-653 (2020).

43 Kim, H.-S. *et al.* Lead iodide perovskite sensitized all-solid-state submicron thin film mesoscopic solar cell with efficiency exceeding 9%. *Scientific reports* **2**, 1-7 (2012).

44 Zhu, C. *et al.* Strain engineering in perovskite solar cells and its impacts on carrier dynamics. *Nature communications* **10**, 1-11 (2019).

45 Xue, D.-J. *et al.* Regulating strain in perovskite thin films through charge-transport layers. *Nature communications* **11**, 1-8 (2020).

46 Rodwell, G. F. & Williamson, A. W. On the coefficients of expansion of the di-iodide of lead, PbI2, and of an alloy of iodide of lead with iodide of silver, PbI2. AgI. *Proceedings of the Royal Society of London* **32**, 540-552 (1881).

47 Rolston, N. *et al.* Engineering stress in perovskite solar cells to improve stability. *Advanced Energy Materials* **8**, 1802139 (2018).

48 Ramirez, C., Yadavalli, S. K., Garces, H. F., Zhou, Y. & Padture, N. P. Thermo-mechanical behavior of organic-inorganic halide perovskites for solar cells. *Scripta Materialia* **150**, 36-41 (2018).

49 Fabini, D. H. *et al.* Reentrant structural and optical properties and large positive thermal expansion in perovskite formamidinium lead iodide. *Angewandte Chemie* **128**, 15618-15622 (2016).

50 Abate, A. *et al.* Lithium salts as "redox active" p-type dopants for organic semiconductors and their impact in solid-state dye-sensitized solar cells. *Physical Chemistry Chemical Physics* **15**, 2572-2579 (2013).

Acknowledgements

Funding: G.L. thanks the support by Research Grants Council of Hong Kong (Grant No. C7018-20G, C5037-18G and GRF 15221320), Shenzhen Science and Technology Innovation Commission (Project No. JCYJ 20200109105003940), the Hong Kong Polytechnic University internal funds: Sir Sze-yuen Chung Endowed Professorship Fund (8-8480) and RISE Fund (Q-CDA5). G.L. thanks Dr. Bolong Huang's for the technical discussion of DFT part. Dr. REN Zhiwei thank PolyU Distinguished Postdoctoral Fellow Scheme (G-YWA9) support. K. L. thanks the Start-up Fund for RAPs under the Strategic Hiring Scheme (1-BD4G) provided by the Hong Kong Polytechnic University, and Guangdong Basic Research Foundation (2020A1515110156). W. Y. thanks the support by Dalian High-level Talents Innovation Support Program (2021RQ120).

Author contributions:

H.Z. and W.Y. contributed equally to this work. G.L. and J-S. H. supervised the work. G. L., H.Z and W.Y conceived the idea, designed the experiments. H.Z and W.Y wrote the paper, and G.L. revised the paper. H.Z. carried out the device fabrication and majority device characterization. W.Y and J.G carried out the AFM measurement, SCLC and FTIR measurement, and revised the manuscript. C.X. and Y.Z carried out

the TEM measurement and structure analysis of supramolecule. M.Q. and X.L. performed ex situ GIWAXS and analyzed the data. Z.R., K.L., Q.L., J-M.H., G.Y., H.T.C., Z.C., and W.Y. assisted in the simulation, characterization of SEM, XRD and optical measurements. Z.W and J-M.H measured the PL. D.S and C.L measured the UPS and XPS. Y.Z. and Z.Z. measured contact angles. All authors discussed the results and commented on the manuscript.

Competing interests: The authors declare that they have no competing interests.

Data and materials availability: All data needed to evaluate the conclusions in the paper are present in the paper and/or the Supplementary Materials.